Research Article | Vol. 32, No. 21 / 7 Oct 2024 / Optics Express 37155

Optics EXPRESS

All-fiber IPDA lidar for CH_4 leakage monitoring using InGaAs/InP single-photon detector

HAOBIN HAN,[1] KENAN WU,[2,5] KEXIN GUO,[1] JIADONG HU,[1] JIAWEI QIU,[1] SAIFEN YU,[1,3] ZHEN ZHANG,[1,3] TENGFEI WU,[4] AND HAIYUN XIA[1,2,3,6]

[1] *School of Atmospheric Physics, Nanjing University of Information Science and Technology, Nanjing 210044, China*
[2] *School of Earth and Space Science, University of Science and Technology of China, Hefei 230026, China*
[3] *National Center of Carbon Metrology (Fujian), Nanping 353011, China*
[4] *Changcheng Institute of Metrology and Measurement, Aviation Industry Corporation of China, Beijing 100095, China*
[5] *wkn924@mail.ustc.edu.cn*
[6] *hsia@ustc.edu.cn*

Abstract: An integrated path differential absorption (IPDA) lidar for CH_4 leakage monitoring is proposed and demonstrated. In the simplified all-fiber optical layout, a homemade InGaAs/InP single-photon detector (SPD) using multi-channel technique with multi-mode fiber coupling is used to increase the maximum count rate and coupling efficiency. The system is calibrated in intensity and frequency domains. Firstly, the fluctuation of the laser power is compensated. Secondly, the dead time, afterpulsing probability and dark counts of the SPD are corrected. A mean relative difference of 0.84% between SPD and PIN photodetector is achieved. Thirdly, non-linear frequency scanning of the laser is measured by homodyne detection and analyzed in joint time-frequency domain. In the symmetry-calibration process, the absorbance spectra of up and down scanning are compared. Maximum difference less than 1% with mean difference of 0.33% is achieved within a span of 4 GHz around the center of absorbance spectrum. Finally, a demonstration experiment over ten days is carried out to analyze the accuracy and stability of the system. A mean deviation of 0.03% with standard deviation of 0.46% is verified at a distance of 12 m and a time resolution of 1 s. By attenuating the laser power from 2 mW to 0.02 mW, the performance of the system is degraded to a mean deviation of 1.32% with standard deviation of 4.33%.

1. Introduction

Global warming is mainly due to greenhouse gas (GHG) emissions from human activities, which has led to numerous extreme weathers across the globe [1–3]. Carbon dioxide (CO_2) and methane (CH_4) are the two most important GHGs, contributing more than 63% and 19% of global radiative forcing, respectively [4]. The monitoring of GHGs is extremely important for GHGs emission reduction and climate change mitigation [5]. In the past decades, numerous device development projects have been proposed for efficiently monitoring GHG emissions, such as CO_2 and CH_4 atmospheric remote monitoring-Flugzeug (CHARM-F) and CH_4 remote sensing Lidar mission (MERLIN) [6,7]. Different from the passive remote sensing methods based on ambient light, the above programs adopt active light source that can continue to work at night and is less susceptible to environment interference [8–12]. Different absorption lidar (DIAL) and integrated path differential absorption (IPDA) lidar are widely used for remote sensing of atmospheric gases in open paths [13–16]. Typically, these systems operating at two nearby wavelengths, with one near the center of the line of target gas and the other at the margin with negligible absorption [17]. Multi-frequency DIAL and IPDA lidar can cover one or even more absorption

#538441 https://doi.org/10.1364/OE.538441
Journal © 2024 Received 2 Aug 2024; revised 13 Sep 2024; accepted 20 Sep 2024; published 30 Sep 2024

Optics EXPRESS

lines allowing the simultaneous detection of multiple atmospheric molecules [18–20]. In our previous work, a multi-frequency DIAL has been demonstrated to simultaneously detect the CO_2 and HDO [21–23], and a coherent DIAL has been demonstrated for measuring CO_2 and wind fields simultaneously [24].

CH_4 has a high global warming potential (GWP) that 27.9 times more potent per kg than CO_2 over 100 years [25]. Monitoring of CH_4 may more urgent due to the dangerous and explosive characteristics, while CH_4 leaks can result in serious and hazardous incidents in some extreme cases that severely jeopardize people's safety [13]. The cost of CH_4 detection equipment is one of the major influences on the ability to fully cover these leak points. Developing innovative technologies to accurately locate and measure CH_4 emissions in an effective and portable manner is extremely important [26,27]. DIAL and IPDA lidar have the advantage of accurately detecting gas concentration with high distance resolution on a large scale of hundreds km^2 [21–24]. However, continuous monitoring of a specific area or a few fixed points using DIAL or IPDA lidar will lead to a higher cost. Tunable diode laser absorption spectroscopy (TDLAS) with simplified structure enables accurate measurement of target gas concentration by rapidly modulating the optical frequency of the laser to cover the specific absorption lines of target gas [28–31]. However, the signal intensity attenuates dramatically with distance is the main reason for limiting long-range detection. Enhancing the response capability of the detector can effectively improve the performance system for path-integrated concentration detection in open path.

Single-photon detectors (SPDs) have the ability to recognize the signal with single-photon intensity, which can overcome the problem that conventional PIN photodetectors cannot recognize weak signals [32]. Superconducting nanowire single-photon detectors (SNSPDs) provides excellent performance of high detection efficiency and broadband response, which have been used for remote sensing [33,34]. However, the practical applications of SNSPDs are limited due to the strict working conditions and the high-cost. Upconversion SPDs exhibit moderate performance and size, but several complex spatial structures are still required [35,36]. Compared with SNSPDs and Upconversion SPDs, InGaAs/InP SPD are more suitable for practical applications with the advantages of small size and low-cost [37,38]. QLM Technology Ltd. has demonstrated a lidar for continuous monitoring of CH_4 based on InGaAs SPD and a technique called TDLidar [39]. Zhu et al. investigated the influences of wedge prism rotation ratios and different environmental conditions on CH_4 leak rate results based on a similar lidar structure [40].

In this work, an all-fiber IPDA lidar with the simplified optical layout is developed for CH_4 leakage monitoring. A homemade InGaAs/InP SPD with multi-channel and multi-mode coupling is used to measure the weak backscattered signal in open path. The intensity and non-linear frequency are corrected for the accurate concentration estimation. A demonstration experiment over ten days is carried out to analyze the accuracy and stability of the system. The preliminary experimental results indicate that the proposed system is reliable for CH_4 continuous monitoring.

2. System design and principle

Schematic diagram of the system for CH_4 detection is shown in Fig. 1. Main parameter values of the experimental system are listed in Table 1. The detection light source adopts a continuous wave (CW) distributed feedback (DFB) laser. An arbitrary waveform generator (AWG) provides the modulated signal for driving the laser working in CW scanning mode. The output power of the laser is weakened by a tunable attenuator, avoiding saturation or even damage of the SPD by the return signal with high intensity. The transmitter is a collimator with a diameter of 25 mm. A dynamic gas calibrator is used to mix the gas with a CH_4/Air ratio of 10^5 ppm. Then, the mixture is flushed into a 40 cm gas cell sealed with optical windows at both ends. The pressure and temperature of the gas cell are 0.16 atm and 298.15 K, respectively. The diffusion medium is a white cement wall at a distance of 12 m from the transmitter. The backscattered signal is coupled into a multi-mode fiber (MMF, 50 µm) by using another collimator with a diameter of 50 mm, which avoids the interference caused by the strongly mirror reflected signal from the transmitter. A in-line optical filter with a bandwidth of 0.3 nm is used to filter out the background light before the SPD.

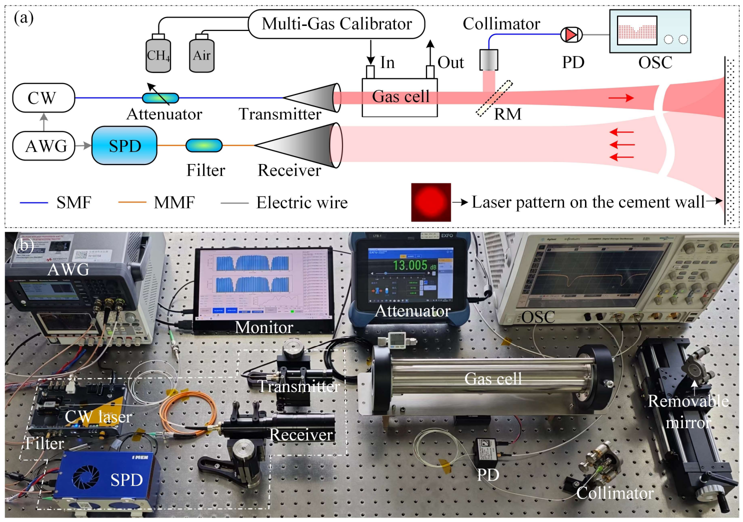

Fig. 1. Schematic diagram (a) and photo (b) of the experimental system for CH_4 detection. AWG, arbitrary waveform generator; SPD, single photon detector; RM, removable mirror; PD, PIN photodetector; OSC, Oscilloscope; SMF, single-mode fiber; MMF, multi-mode fiber.

Table 1. Key parameters of the system

Sub-system		Parameter value
CW laser	Optical frequency span	181.283 THz ±5 GHz
	Maximum power	40 mW
	Linewidth	200 kHz
InGaAs/InP SPD	Detection efficiency	5% @ 1650 nm
	DT	200 ns
	AP	~12%
	DC	~500 cps
PIN Photodetector	Detection efficiency	75%
	Dark current	0.1 nA
	Noise Equivalent power	10^{-15} W/Hz$^{1/2}$
Transmitter	Diameter	25 mm
	Focal length	100 mm
Receiver	Diameter	50 mm
	Focal length	200 mm

The detection efficiency of the SPD is spectrum-dependent, about 15% at 1550 nm but only 5% at 1650 nm under the same conditions [41]. The dead time (DT), afterpulsing probability (AP) and dark counts (DC) of the SPD are 200 ns, ~12% and ~500 cps, respectively. Multi-channel technology is used to increase the maximum count rate of the SPD, which avoiding the single-channel SPD tends to operate in the non-linear response region under strong near-field signals and improving the dynamic detection range of the SPD.

A collimator couples the light reflected by a removable mirror into a PIN photodetector and recorded by an Oscilloscope. Figure 2 shows the signals detected by a conventional PIN photodetector including the modulated signal for CW scanning, baseline and the transmission after CH_4 absorption. A square wave signal with a frequency of 100 kHz and a duty cycle of 50% is used as the modulating signal to scan the optical frequency of CW laser up and down across the absorbance spectrum of CH_4 around 181.283 THz [42]. The entire CH_4 absorption cross-section is obtained in both up and down scanning processes.

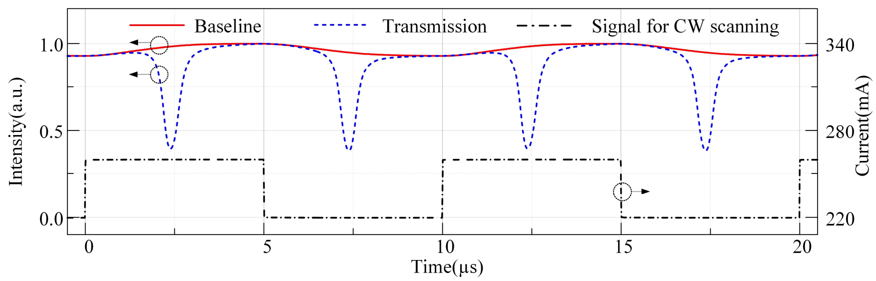

Fig. 2. Signals detected by a PIN photodetector, including the signal for optical frequency tuning, baseline of laser intensity without CH_4 absorption and transmission after CH_4 absorption.

The principle of absorbance spectroscopy is based on the Beer-Lambert law [43,44], which can be expressed as

$$\alpha(v) = -\ln\left(\frac{I_t(v)}{I_0(v)}\right) = S(T)XPL\phi(v), \tag{1}$$

where $\alpha(v)$ is the absorbance at optical frequency v, $I_t(v)$ is the intensity of transmission through the gas cell, $I_0(v)$ is the laser intensity, $S(T)$ is the spectral line intensity related to the temperature T, X is the gas concentration, P is the gas pressure and L is the optical path length of gas absorption. $\phi(v)$ represents the normalized line profile function at a specific temperature and pressure, which meet the relationship of $\int_{-\infty}^{\infty} \phi(v)dv \equiv 1$. According to the temperature and pressure of CH_4 cell, triple-peak Voigt line profile function is used to fit the total absorbance spectrum of the CH_4 at 181.283 THz consists of three absorption lines [21,45], which can be expressed as

$$\phi(v) = \sum_{i=1}^{3} \phi_i(v) = \sum_{i=1}^{3} A_i \frac{2y_i^2}{\omega_{Li}\pi^{3/2}} \int_{-\infty}^{\infty} \frac{e^{-t^2}}{y_i^2 + (x_i - t)^2} dt, \tag{2}$$

where $x_i = (4\ln 2)^{1/2}(v - v_{ci})/\omega_{Gi}$ and $y_i = (\ln 2)^{1/2}\omega_{Li}/\omega_{Gi}$ are given for simplicity. A_i is the Voigt area, ω_{Li} and ω_{Gi} are the Lorentzian full-width at half-maximum (FWHM) and Gaussian FWHM, respectively, v_{ci} is the center frequency of the absorption line. Mixed absorbance area A can be obtained by integrating the fitted absorbance spectrum, which can be expressed as

$$A = \int_{-\infty}^{\infty} \alpha(v)dv = S(T)XPL. \tag{3}$$

As a result, path-integrated gas concentration C can be obtained as

$$C = XL = \frac{A}{S(T)P}. \tag{4}$$

Optics EXPRESS

3. Experiment

Periodic intensity fluctuation during the scanning is shown in Fig. 2, which can be compensated for by recording the baseline. In addition, the intensity errors caused by the SPD and the non-linear frequency of the laser should be corrected before the concentration estimation. A flowchart of data processing and CH_4 concentration estimation is shown in Fig. 3.

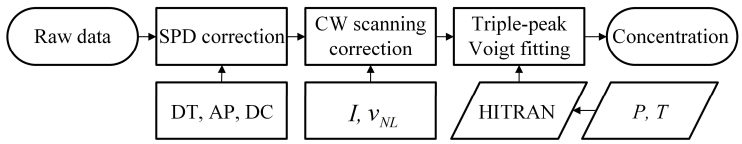

Fig. 3. Flowchart of CH_4 concentration detection. I, Intensity; v_{NL}, non-linear frequency; P, pressure; T, temperature.

Step 1: After obtaining the raw data of the baseline and transmission by SPD. The SPD-correction is used to sequentially correct the intensity errors caused by DT, AP and DC.

Step 2: The fluctuation of the laser power is compensated by using Eq. (1). Then, the non-linear frequency during CW scanning is measured by homodyne detection and analyzed in joint time-frequency domain.

Step 3: Triple-peak Voigt model is performed to fit the CH_4 absorbance spectra consisting of three absorption lines. According to the temperature and pressure of the CH_4 cell, several HITRAN databased initial conditions are used in the fitting process, including the strength of gas absorption lines, relative frequency positions and FWHM.

Step 4: The path-integrated concentration of CH_4 can be estimated from the aera of the fitted absorbance spectra.

3.1. SPD correction

DT, AP and DC are the key parameters of SPDs, and these parameters will be optimized according to the application requirements before actual application. However, due to the interaction between these parameters, photon counts errors still exist under the compromise optimization approach. Details about the SPD correction algorithm can be found in the previous work [46].

Figure 4 shows the baseline of laser intensity and the transmission after CH_4 absorption detected by the SPD before and after correction with time resolution of 1 s. The output power of laser is significantly attenuated to ensure the return signal intensity of 5.4 Mcps during the calibration and demonstration experiments, which allows the SPD operating in the linear response region and guarantees the accuracy of the SPD-correction method. It should be noted that all of the experiments are conducted in an indoor laboratory that the ambient CH_4 concentration is negligible for experimental results. The baseline is measured by directly connecting the fiber into the SPD without the absorption of CH_4, and the raw data are sequentially corrected for DT, AP and DC, as shown in Fig. 4(a). Figure 4(b) shows the raw data and the SPD-corrected results of the transmission through the CH_4 cell, while the detection distance is 12 m and the output power of the laser is 2 mW. Comparing the raw data and the results corrected by SPD-correction in Figs. 4(a) and 4(b), DT and AP cause a large error on the photon counts, while the influence caused by DC can be neglected. The CH_4 absorbance spectrum detected by PIN photodetector is used as a reference for comparison, as shown in Fig. 4(c). The SPD-corrected absorbance curve resulted in significantly higher absorbance compared to the raw data, specifically the top point of CH_4 absorbance is 0.77 and 0.92 before and after correction. The absorbance after SPD-correction is in high agreement with the results detected by PIN photodetector, which indicates that the SPD-correction method effectively corrects the intensity errors caused by DT, AP and DC on photons counts. Figure 4(d) shows the differences of absorbance measured by SPD before and after correction in contrast to the curve measured by PIN photodetector. In the larger portion of the absorbance as indicated by yellow shading areas in Figs. 4(c) and 4(d), the maximum difference between SPD raw data and PIN photodetector-measured one is larger than 16.4% while the mean difference is 4.95%. After SPD-correction, the maximum difference and mean difference can be decreased to 2.6% and 0.84%. Note that, the residual relative differences after SPD-correction show symmetric distribution about the centers. As we pointed out earlier, this phenomenon is due to the different sampling methods between the digital and analog detection [47], where the SPD averages the photon counts over a period of time (50 ns), while the PIN photodetector samples the signal at 1 GSa/s.

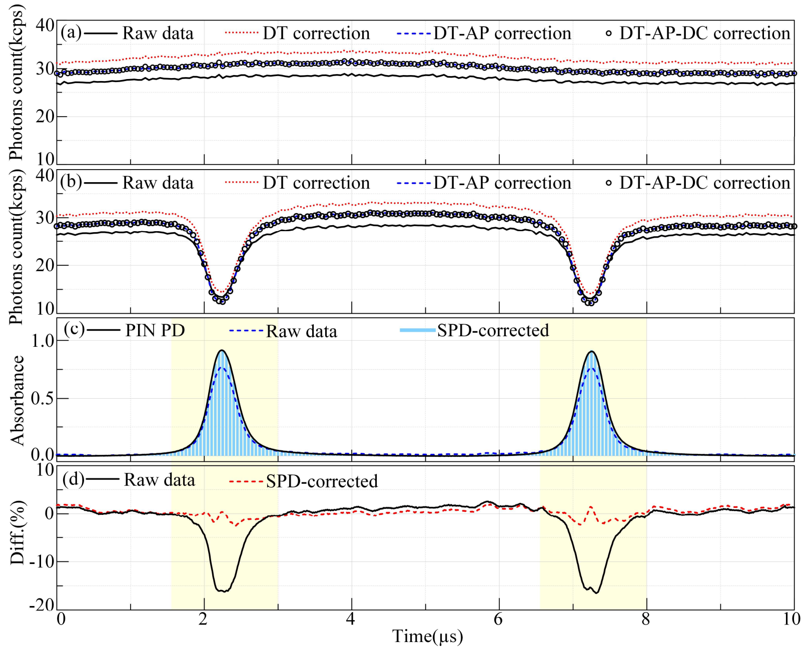

Fig. 4. (a) Laser baseline and (b) transmission signal detected by SPD and sequentially corrected for DT, AP, and DC. (c) Comparison of CH_4 absorbance detected by PIN photodetector and SPD. (d) Given the results measured by PIN PD as a reference, the differences of absorbance using SPD before and after SPD-correction. Diff.: difference.

3.2. Non-linear frequency correction

The modulating signal drives the current fed into the laser, affecting the temperature and the carrier concentration in the gain medium, both of which will change the optical frequency of laser [48]. The carrier concentration in the active layer of the laser increases rapidly with a step increase of the modulated current, resulting in an accelerated change in optical frequency and gradually slows down to a steady-state value due to thermal effects [49]. As a result, the gas absorption line profile is distorted, since the optical frequency of laser varies nonlinearly versus time during scanning.

An unbalanced Mach-Zender interferometer (MZI) is served as a frequency discriminator to measure the non-linear frequency scanning [50], as shown in Fig. 5. A CH_4 cell with a fiber pigtail is connected in front of the MZI, and the position of the CH_4 absorption peak can be found. This position will be used as a reference for absolute optical frequency for correcting non-linear frequency. The unbalanced MZI consists of two 50:50 couplers (C1, C2) and a length of delay line (the length difference is 1 m between the two arms). The beat frequency is measured by a PIN photodetector with a bandwidth of 1 GHz and recorded by an OSC at sampling rate of 1 GSa/s.

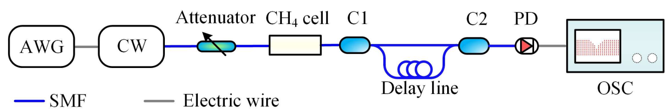

Fig. 5. Schematic of the unbalanced MZI for homodyne detection. C, Coupler.

The time delay introduced in two arms of MZI is ~5 ns that is much smaller than the scanning period of 5 μs, thus the beat frequency $f(t)$ can be expressed as the time derivative of optical frequency

$$f(t) = \frac{dv(t)}{dt}\tau, \tag{5}$$

where $v(t)$ is the instantaneous optical frequency of laser during CW scanning, τ is the time delay difference introduced in MZI. Joint time-frequency analysis (JTFA) maps a two-dimensional time function into a three-dimensional time-frequency distribution to characterize the intensity of signals at different times and frequencies, which has been widely applied in the fields of machinery inspection [51], seismic exploration [52] and lidar [53]. Based on advantage of the refined processing for signal in time and frequency, JTFA is used to process the beat frequency to obtain the instantaneous optical frequency variation. According to the optical frequency of the gas absorption peak and corresponding time position, the exact instantaneous optical frequency can be estimated by integrating the beat frequency, which is given as

$$v(t) = v_0 \pm R\int_{t_0}^{t} f(t)dt, \tag{6}$$

where v_0 is the optical frequency of the gas absorption peak. In this work $R = 0.2$ is the ratio coefficient of sampling interval t_{sa} and delay time τ. Different from the conventional interferometric approaches only the frequency information at the interferometric peak or valley positions can be obtained, the instantaneous frequency change at each sampling point can be estimated by analyzing the beat frequency in joint time-frequency domain. As a result, more details of the frequency variations can be estimated by using JTFA thus enabling more accurate non-linear frequency corrections.

Figure 6 illustrates the beat frequency signals and the results processed by JTFA. Figure 6(a) is the time-domain interferogram of two same CW scanning signal obtained by homodyne detection with different delay time, and the absorption information of CH_4 is contained within the intensity of beat frequency signal. The effects of high-frequency and low-frequency noises are eliminated by a band-pass filter. The filtered beat frequency is processed by the JTFA with Choi-Williams distribution (CWD), then the beat frequency $f(t)$ i.e. instantaneous optical frequency change can be obtained, as shown in Fig. 6(b). The black solid line represents the maximum intensity of beat frequency signal at the corresponding time sampling point, the corresponding vertical coordinate is the instantaneous optical frequency change. It can be clearly seen that the optical frequency of the laser varies nonlinearly with time, accelerating at the instant when the high and low level of modulating signal changes and slowing down at the point where closes to the CH_4 absorption peak. As a result, the absorbance spectrum in the time domain exhibits a distinctly asymmetric structure, as shown in Figs. 7(a) and 7(b). The total optical frequency range of CW scanning and the real optical frequency can be obtained by integrating the beat frequency at every time sampling points according to Eq. (6). Figure 6(c) shows the real optical frequency $v(t)$ during CW scanning. The optical frequency span in the scanning is about 10 GHz.

Optics EXPRESS

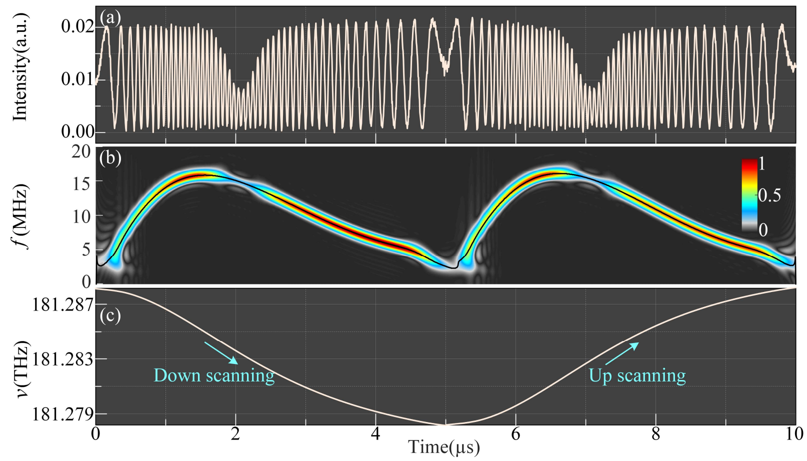

Fig. 6. (a) Temporal interferogram. (b) Beat frequency $f(t)$ processed by the JTFA with CWD. (c) Optical frequency $v(t)$ during CW scanning.

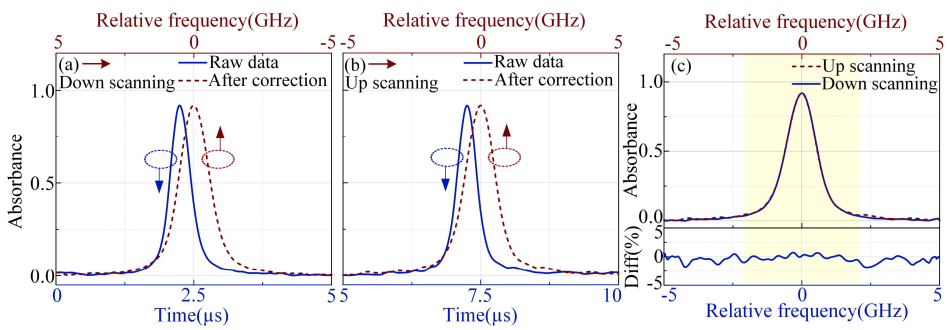

Fig. 7. The absorbance spectra before and after non-linear frequency correction in (a) down and (b) up scanning. (c) Comparison of absorbance spectra in up and down scanning. The subfigure below (c) is the difference between the both absorbance spectra.

Figures 7(a) and 7(b) show the absorbance spectra before and after non-linear frequency correction in down and up scanning, respectively. A symmetry-calibration process that comparing the absorbance spectra of up and down scanning is used to verify the accuracy the correction at this step, as shown in Fig. 7(c). The maximum difference is less than 1% with mean difference of 0.33% is achieved within a span of 4 GHz around the center of absorbance spectrum, which indicating that the non-linear frequencies during scanning are well corrected.

3.3. Accuracy and stability

After correcting for intensity errors due to photon counts and non-linear frequencies during scanning, triple-peak Voigt model is used in the fitting process of CH_4 absorbance spectra nearby 181.283 THz consists of three absorption lines. The final absorbance spectra used for fitting are the average of both spectra in up and down scanning. The Levenberg-Marquardt method is used to achieve the numerical least-squares optimization of the Voigt fitting.

Figure 8(a) shows the ten typical triple-peak Voigt fitting results of CH_4 absorbance spectrum at a detection distance of 12 m, while the signal intensity is 5.4 Mcps and the time resolution is 1 s. The absorbance spectra corresponding to the three absorption lines and the mixed one show a high degree of agreement at strong signal intensity. The standard deviation of residual between the corrected results and fitting results is 0.4%. The backscattered signal received in the frequency of v and at a range of R can be expressed by [54]

$$P(v,R) = \frac{K\beta(v,R)T_r^2(v,R)}{R^2}, \tag{7}$$

where K is the constant of lidar system, $\beta(v,R)$ is the volume backscatter coefficient, $T_r(v,R)$ is the transmittance of atmosphere. According to the Eq. (7), the backscattered signal through the atmosphere decays proportionally to the square of the distance. At the real detection distance of 12 m, the laser output power is attenuated by 20 dB from 2 mW to 0.02 mW, which leading the signal intensity decreasing to 54 kcps. This signal intensity corresponds to the detection distance of 120 m. Figure 8(b) shows the triple-peak Voigt fitting results of the absorbance spectra, in which the weak signals lead to large fluctuation in the residual curves with a maximum of 8.51%.

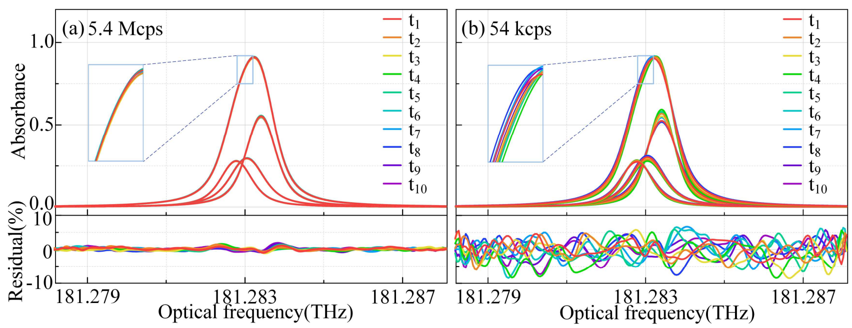

Fig. 8. Results of ten typical tests after triple-peak Voigt fitting at two different signal intensities with a time resolution of 1 s, (a) signal intensity of 5.4 Mcps with the detection distance of 12 m, (b) signal intensity of 54 kcps. The subfigures below (a) and (b) are residuals between the results of experiment and fitting. t, test.

To further validate the accuracy and stability of the system, continuous observations over 10 days are carried out at two different signal intensities. Figure 9 shows the 40 groups of test results both in the intensity of 5.4 Mcps and 54 kcps, while the test is carried out every 3 hours and each group of tests contain 20 results. The concentration of the CH_4 cell is 10^5 ppm with the optical path of 40 cm, which corresponding path-integrated concentration is 4×10^4 ppm·m. Figure 9(a) shows the path-integrated concentration measured at a signal intensity of 5.4 Mcps with a time resolution of 1 s. The measurements results show good consistency, where mean deviation of 10.47 ppm·m (0.03%) with standard deviation of 182.22 ppm·m (0.46%) is achieved. Figure 9(b) shows the results measured at the signal intensity about 54 kcps at a time resolution of 1 s. The mean deviation and the standard deviation are degraded to 529.04 ppm·m (1.32%) and 1732.27 ppm·m (4.33%), respectively. The larger concentration deviation is due to the lower signal-to-noise ration of the weak signal intensity, and the results in weak signal intensity can be used to simulated the return signal from the detection distance of 120 m or the objects with weak reflection coefficient. It should be noticed that the relative output power is only the 1/20 of the maximum power, which indicates that the accuracy can be improved by increasing the laser power in field test.

Optics EXPRESS

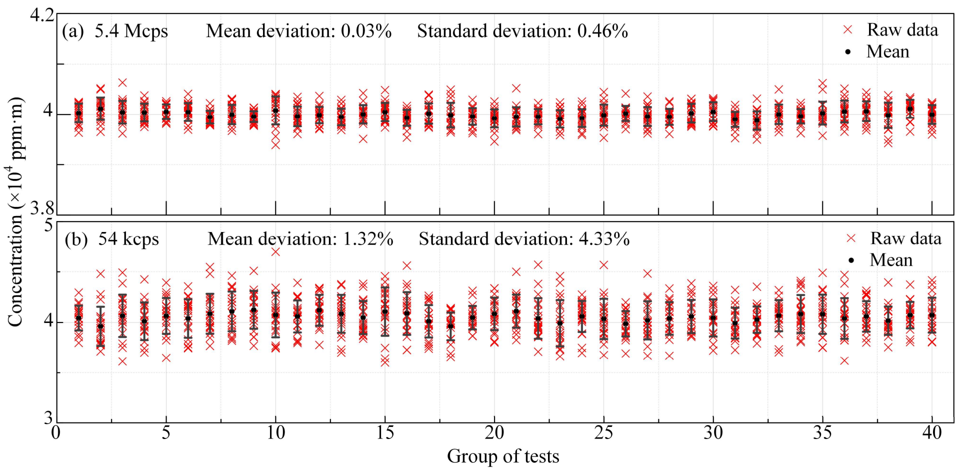

Fig. 9. Continuous observation over 10 days of CH_4 path-integrated concentration detection. (a) Detection distance of 12 m, with the signal intensity of 5.4 Mcps and a time resolution of 1 s. (b) Simulated detection distance of 120 m by attenuating the signal intensity to 54 kcps with a time resolution of 1 s. The time interval between adjacent tests is 3 hours and each test contained 20 results.

4. Conclusion

An IPDA lidar with simplified all-fiber optical layout are demonstrated for CH_4 leakage monitoring. For the accurate concentration estimated, the intensity is corrected by SPD-correction and the non-linear frequency is corrected by homodyne detection and JTFA. The accuracy and stability are verified by a continuous observation over ten days. A mean deviation of 0.03% with standard deviation of 0.46% is achieved at a distance of 12 m and a time resolution of 1 s. The detection performance with weak signal intensity that attenuated by 20 dB is verified with a mean deviation of 1.32% and a standard deviation of 4.33%.

The preliminary experiment results demonstrated that the proposed all-fiber IPDA lidar system for CH_4 detection is reliable. In the near future, several measures will be applied to further enhance the performance of system. The linear frequency variation during CW scanning can be realized by using pre-distortion for modulated current [55,56], which will reduce the errors caused by non-linear frequency variations. The distance to the target can be realized by integrating a small-sized and low-cost ranging lidar, and more optical power can be used for improve the detection distance. The laser, SPD, transmitter and receiver framed by the white dashed line in Fig. 1(b) will be integrated, thus the system can be used as a portable lidar. In addition, benefiting from the wide response of InGaAs/InP SPD in the near-infrared band, the improved system can be adapted to the continuous monitoring of other gas leaks, such as H_2S, CO, NH_3, by integrating more laser sources using optical switches.

Funding. National Natural Science Foundation of China (42305147); National Key Research and Development Program of China (2022YFF0606400).

Disclosures. The authors declare that there are no conflicts of interest related to this article.

Data availability. Data underlying the results presented in this paper are not publicly available at this time but may be obtained from the authors upon reasonable request.

References

1. H. Lee, K. Calvin, D. Dasgupta, *et al.*, "Climate Change 2023: Synthesis Report," in *Contribution of Working Groups I, II and III to the Sixth Assessment Report of the Intergovernmental Panel on Climate Change* (IPCC, 2023).

2. P. M. Forster, C. J. Smith, T. Walsh, *et al.*, "Indicators of Global Climate Change 2022: annual update of large-scale indicators of the state of the climate system and human influence," Earth Syst. Sci. Data **15**(6), 2295–2327 (2023).
3. X. Bi, Z. Gao, X. Deng, *et al.*, "Seasonal and diurnal variations in moisture, heat, and CO_2 fluxes over grassland in the tropical monsoon region of southern China," J. Geophys. Res. **112**(D10), D10106 (2007).
4. S. Montzka, *The NOAA Annual Greenhouse Gas Index*, NOAA Global Monitoring Laboratory, https://gml.noaa.gov/aggi/aggi.html (last access: 2 June 2023).
5. G. Han, Z. Pei, T. Shi, *et al.*, "Unveiling Unprecedented Methane Hotspots in China's Leading Coal Production Hub: A Satellite Mapping Revelation," Geophys. Res. Lett. **51**(10), e2024GL109065 (2024).
6. A. Amediek, G. Ehret, A. Fix, *et al.*, "CHARM-F—a new airborne integrated-path differential-absorption lidar for carbon dioxide and methane observations: measurement performance and quantification of strong point source emissions," Appl. Opt. **56**(18), 5182–5197 (2017).
7. G. Ehret, P. Bousquet, C. Pierangelo, *et al.*, "MERLIN: A French-German space lidar mission dedicated to atmospheric methane," Remote Sens. **9**(10), 1052 (2017).
8. D. W. T. Griffith, R. Leuning, O. T. Denmead, *et al.*, "Air-land exchanges of CO_2, CH_4 and N_2O measured by FTIR spectrometry and micrometeorological techniques," Atmos. Environ. **36**(11), 1833–1842 (2002).
9. C. Clerbaux, A. Boynard, L. Clarisse, *et al.*, "Monitoring of atmospheric composition using the thermal infrared IASI/MetOp sounder," Atmos. Chem. Phys. **9**(16), 6041–6054 (2009).
10. G. A. Wagner and D. F. Plusquellic, "Ground-based, integrated path differential absorption LIDAR measurement of CO_2, CH_4, and H_2O near 1.6 µm," Appl. Opt. **55**(23), 6292–6310 (2016).
11. G. Gibson, B. van Well, J. Hodgkinson, *et al.*, "Imaging of methane gas using a scanning, open-path laser system," New J. Phys. **8**(2), 26 (2006).
12. G. M. Gibson, B. Q. Sun, M. P. Edgar, *et al.*, "Real-time imaging of methane gas leaks using a single-pixel camera," Opt. Express **25**(4), 2998–3005 (2017).
13. N. Cézard, S. Le Mehaute, J. Le Gouet, *et al.*, "Performance assessment of a coherent DIAL-Doppler fiber lidar at 1645 nm for remote sensing of methane and wind," Opt. Express **28**(15), 22345–22357 (2020).
14. E. Cadiou, D. Mammez, J. B. Dherbecourt, *et al.*, "Atmospheric boundary layer CO_2 remote sensing with a direct detection LIDAR instrument based on a widely tunable optical parametric source," Opt. Lett. **42**(20), 4044–4047 (2017).
15. G. Han, Y. Huang, T. Shi, *et al.*, "Quantifying CO_2 emissions of power plants with Aerosols and Carbon Dioxide Lidar onboard DQ-1," Remote Sens. Environ. **313**(1), 114368 (2024).
16. X. Zhang, M. Zhang, L. Bu, *et al.*, "Simulation and Error Analysis of Methane Detection Globally Using Spaceborne IPDA Lidar," Remote Sens. **15**(13), 3239 (2023).
17. J. Hamperl, J. B. Dherbecourt, M. Raybaut, *et al.*, "Range-resolved detection of boundary layer stable water vapor isotopologues using a ground-based 1.98 µm differential absorption LIDAR," Opt. Express **30**(26), 47199–47215 (2022).
18. J. B. Abshire, A. K. Ramanathan, H. Riris, *et al.*, "Airborne measurements of CO_2 column concentrations made with a pulsed IPDA lidar using a multiple-wavelength-locked laser and HgCdTe APD detector," Atmos. Meas. Tech. **11**(4), 2001–2025 (2018).
19. W. P. Rosas and N. Cézard, "Greenhouse gas monitoring using an IPDA lidar based on a dual-comb spectrometer," Opt. Express **32**(8), 13614–13627 (2024).
20. G. A. Wagner and D. F. Plusquellic, "Multi-frequency differential absorption LIDAR system for remote sensing of CO_2 and H_2O near 1.6 µm," Opt. Express **26**(15), 19420–19434 (2018).
21. S. Yu, Z. Zhang, M. Li, *et al.*, "Multi-frequency differential absorption lidar incorporating a comb-referenced scanning laser for gas spectrum analysis," Opt. Express **29**(9), 12984–12995 (2021).
22. S. Yu, Z. Zhang, H. Xia, *et al.*, "Photon-counting distributed free-space spectroscopy," Light: Sci. Appl. **10**(1), 212 (2021).
23. B. Yue, S. Yu, M. Li, *et al.*, "Local-scale horizontal CO_2 flux estimation incorporating differential absorption lidar and coherent doppler wind lidar," Remote Sens. **14**(20), 5150 (2022).
24. S. Yu, K. Guo, S. Li, *et al.*, "Three-dimensional detection of CO_2 and wind using a 1.57 µm coherent differential absorption lidar," Opt. Express **32**(12), 21134–21148 (2024).
25. K. A. Mar, C. Unger, L. Walderdorff, *et al.*, "Beyond CO_2 equivalence: The impacts of methane on climate, ecosystems, and health," Environ. Sci. Policy **134**, 127–136 (2022).
26. J. Wang, L. P. Tchapmi, A. P. Ravikumar, *et al.*, "Machine vision for natural gas methane emissions detection using an infrared camera," Appl. Energy **257**, 113998 (2020).
27. K. J. Nutt, N. Hempler, G. T. Maker, *et al.*, "Developing a portable gas imaging camera using highly tunable active-illumination and computer vision," Opt. Express **28**(13), 18566–18576 (2020).
28. Q. Wang, P. Sun, Z. Zhang, *et al.*, "Method of adaptive wide dynamic range gas concentration detection based on optimized direct absorption spectroscopy," Opt. Express **31**(10), 16770–16780 (2023).
29. J. Shemshad, S. M. Aminossadati, and M. S. Kizil, "A review of developments in near infrared methane detection based on tunable diode laser," Sens. Actuators, B **171-172**, 77–92 (2012).
30. J. Jiang, M. Zhao, G. Ma, *et al.*, "TDLAS-Based Detection of Dissolved Methane in Power Transformer Oil and Field Application," IEEE Sens. J. **18**(6), 2318–2325 (2018).

Optics EXPRESS

31. C. Hansemann, M. Bonarens, J. Emmert, *et al.*, "Towards a spatially resolved, single-ended TDLAS system for characterizing the distribution of gaseous species," Sci. Rep. **14**(1), 11708 (2024).
32. R. H. Hadfield, J. Leach, F. Fleming, *et al.*, "Single-photon detection for long-range imaging and sensing," Optica **10**(9), 1124–1141 (2023).
33. Y. Guan, H. Li, L. Xue, *et al.*, "Lidar with superconducting nanowire single-photon detectors: Recent advances and developments," Opt. Laser. Eng. **156**, 107102 (2022).
34. M. Li, Y. Wu, J. Yuan, *et al.*, "Stratospheric aerosol lidar with a 300 µm diameter superconducting nanowire single-photon detector at 1064 nm," Opt. Express **31**(2), 2768–2779 (2023).
35. L. Meng, A. Fix, M. Wirth, *et al.*, "Upconversion detector for range-resolved DIAL measurement of atmospheric CH_4," Opt. Express **26**(4), 3850–3860 (2018).
36. H. Xia, G. Shentu, M. Shangguan, *et al.*, "Long-range micro-pulse aerosol lidar at 1.5 µm with an upconversion single-photon detector," Opt. Lett. **40**(7), 1579–1582 (2015).
37. M. Shangguan, Y. Guo, Z. Liao, *et al.*, "Sensing profiles of the volume scattering function at 180° using a single-photon oceanic fluorescence lidar," Opt. Express **31**(24), 40393–40410 (2023).
38. P. Jiang, H. Xia, J. Hu, *et al.*, "Estimation of atmospheric refractive index structure constant using an InGaAs/InP single-photon detector," Opt. Lett. **48**(23), 6104–6107 (2023).
39. J. Titchener, D. Millington-Smith, C. Goldsack, *et al.*, "Single-photon Lidar gas imagers for practical and widespread continuous methane monitoring," Appl. Energy **306**, 118086 (2022).
40. S. Zhu, S. Liu, G. Tang, *et al.*, "Simulation evaluation of a single-photon laser methane remote sensor for leakage rate monitoring," Opt. Express **32**(7), 10962–10978 (2024).
41. G. Ribordy, N. Gisin, O. Guinnard, *et al.*, "Photon counting at telecom wavelengths with commercial InGaAs/InP avalanche photodiodes: current performance," J. Mod. Opt. **51**(9-10), 1381–1398 (2004).
42. I. E. Gordon, L. S. Rothman, R. J. Hargreaves, *et al.*, "The HITRAN2020 molecular spectroscopic database," J. Quant. Spectrosc. Radiat. Transfer **277**, 107949 (2022).
43. R. Hanson, R. Spearrin, and C. Goldenstein, *Spectroscopy and Optical Diagnostics for Gases* (Springer, 2015).
44. T. Strahl, J. Herbst, A. Lambrecht, *et al.*, "Methane leak detection by tunable laser spectroscopy and mid-infrared imaging," Appl. Opt. **60**(15), C68–C75 (2021).
45. H. Xia, D. Sun, Y. Yang, *et al.*, "Fabry-Perot interferometer based Mie Doppler lidar for low tropospheric wind observation," Appl. Opt. **46**(29), 7120–7131 (2007).
46. C. Yu, M. Shangguan, H. Xia, *et al.*, "Fully integrated free-running InGaAs/InP single-photon detector for accurate lidar applications," Opt. Express **25**(13), 14611–14620 (2017).
47. J. Qiu, H. Xia, X. Dou, *et al.*, "Optimization of scanning Fabry-Perot interferometer in the high spectral resolution lidar for stratospheric temperature detection," Opt. Eng. **55**(8), 084107 (2016).
48. H. Shalom, A. Zadok, M. Tur, *et al.*, "On the various time constants of wavelength changes of a DFB laser under direct modulation," IEEE J. Quantum Electron. **34**(10), 1816–1822 (1998).
49. A. A. Saavedra, R. Passy, and J. P. von der Weid, "Thermal drift in wavelength-switching DFB and DBR lasers," Electron. Lett. **33**(9), 780–781 (1997).
50. H. Xia and C. Zhang, "Ultrafast ranging lidar based on real-time Fourier transformation," Opt. Lett. **34**(14), 2108–2110 (2009).
51. J. Urbanek, T. Barszcz, and J. Antoni, "A two-step procedure for estimation of instantaneous rotational speed with large fluctuations," Mech. Syst. Signal. Pr. **38**(1), 96–102 (2013).
52. D. Song, Z Chen, Y. Ke, *et al.*, "Seismic response analysis of a bedding rock slope based on the time-frequency joint analysis method: a case study from the middle reach of the Jinsha River, China," Eng. Geol. **274**(5), 105731 (2020).
53. C. Wang, H. Xia, Y. Liu, *et al.*, "Spatial resolution enhancement of coherent Doppler wind lidar using joint time-frequency analysis," Opt. Commun. **424**, 48–53 (2018).
54. T. Fujii and T. Fukuchi, *Laser Remote Sensing* (CRC Press, 2005).
55. X. Zhang, J. Pouls, and M. Wu, "Laser frequency sweep linearization by iterative learning pre-distortion for FMCW LiDAR," Opt. Express **27**(7), 9965–9974 (2019).
56. P. Li, Y. Zhang, and J. Yao, "Rapid Linear Frequency Swept Frequency-Modulated Continuous Wave Laser Source Using Iterative Pre-Distortion Algorithm," Remote Sens. **14**(14), 3455 (2022).